

CHANDRA COUNTERPARTS OF CANDELS GOODS-S SOURCES.

N. CAPPELLUTI^{1,2,3}, A. COMASTRI¹, A. FONTANA⁴, G. ZAMORANI¹, R. AMORIN⁴, M. CASTELLANO⁴, E. MERLIN⁴, P. SANTINI⁴, D. ELBAZ⁵, C. SCHREIBER⁵, X. SHU^{5,10}, T. WANG^{5,11}, J. S. DUNLOP⁶, N. BOURNE⁶, V. A. BRUCE⁶, F. BUITRAGO^{6,12,13}, MICHAŁ J. MICHAŁOWSKI⁶, S. DERRIERE⁷, H. C. FERGUSON⁸, S. M. FABER⁹, F. VITO^{1,14}

ABSTRACT

Improving the capabilities of detecting faint X-ray sources is fundamental to increase the statistics on faint high- z AGN and star-forming galaxies. We performed a simultaneous Maximum Likelihood PSF fit in the [0.5-2] keV and [2-7] keV energy bands of the 4 Ms *Chandra* Deep Field South (CDFS) data at the position of the 34930 CANDELS H-band selected galaxies. For each detected source we provide X-ray photometry and optical counterpart validation. We validated this technique by means of a raytracing simulation. We detected a total of 698 X-ray point-sources with a likelihood $\mathcal{L} > 4.98$ (i.e. $> 2.7\sigma$). We show that the prior knowledge of a deep sample of Optical-NIR galaxies leads to a significant increase of the detection of faint (i.e. $\sim 10^{-17}$ cgs in the [0.5-2] keV band) sources with respect to "blind" X-ray detections. By including previous X-ray catalogs, this work increases the total number of X-ray sources detected in the 4 Ms CDFS, CANDELS area to 793, which represents the largest sample of extremely faint X-ray sources assembled to date. Our results suggest that a large fraction of the optical counterparts of our X-ray sources determined by likelihood ratio actually coincides with the priors used for the source detection. Most of the new detected sources are likely star-forming galaxies or faint absorbed AGN. We identified a few sources sources with putative photometric redshift $z > 4$. Despite the low number statistics and the uncertainties on the photo- z , this sample significantly increases the number of X-ray selected candidate high- z AGN.

Subject headings: galaxies: active— galaxies: active, (galaxies:) quasars: supermassive black holes, galaxies: high-redshift

1. INTRODUCTION

The scientific return of deep X-ray surveys is maximized in those regions of the sky intensively covered by longer wavelength observations. For example, the study of the accretion and star formation processes and their

cosmic evolution is routinely performed combining observations obtained in the X-ray and in the optical and near infrared bands. It is widely accepted that all bulged galaxies host a Super Massive Black Hole (SMBH) in their center and a fraction of them, roughly of the order of a few percent, show some kind of nuclear activity. Luminous X-ray emission is a clear signature of nuclear activity produced in the vicinity of the central black hole (BH). Also non-active galaxies emit X-ray light, at luminosities much lower than that produced by AGN, due to stellar driven processes such as accretion onto binaries and supernovae remnants. As a consequence, X-ray luminosity is also a probe of the Star Formation Rate (SFR, Fabbiano 1989; Ranalli et al. 2005; Mineo et al. 2012; Basu-Zych et al. 2013). Together with Clusters of Galaxies, Active Galactic Nuclei (AGN) and Star-forming galaxies (SFG) are the three main ingredients of the extragalactic Cosmic X-ray Background (CXB). *Chandra* and XMM-*Newton* surveys were able to resolve a large fraction of the extragalactic CXB in discrete sources. The yet unresolved fraction is thought to be made by a mix of faint SFG at moderate to high redshifts and low luminosity AGN.

The selection of sizable samples of faint AGN is fundamental to understand AGN evolution and to constrain models of SMBH formation especially at high- z . So far X-ray surveys have sampled the bright end ($L_X \geq 10^{43}$) of the AGN X-ray Luminosity Function (XLF) up to $z \sim 5$ (see e.g. Ueda et al. 2014; Hasinger 2008; Aird et al. 2010; Ebrero et al. 2009; Miyaji et al. 2015; Vito et al. 2014). At higher redshifts only a handful of very bright AGN powered by massive BH are known, but the low luminosity tail of the XLF remains unknown. These

¹ INAF - Osservatorio Astronomico di Bologna, Via Ranzani 1, I - 40127, Bologna, Italy

² Department of Physics, Yale University, P.O. Box 208121, New Haven, CT 06520, USA

³ Yale Center for Astronomy & Astrophysics, Physics Department, P.O. Box 208120, New Haven, CT 06520, USA

⁴ INAF - Osservatorio Astronomico di Roma, Via Frascati 33, I - 00040 Monte Porzio Catone (RM), Italy

⁵ Laboratoire AIM-Paris-Saclay, CEA/DSM/Irfu - CNRS - Université Paris Diderot, CEA-Saclay, pt courrier 131, F-91191 Gif-sur-Yvette, France

⁶ SUPAScottish Universities Physics Alliance, Institute for Astronomy, University of Edinburgh, Royal Observatory, Edinburgh, EH9 3HJ, U.K.

⁷ Observatoire astronomique de Strasbourg, Université de Strasbourg, CNRS, UMR 7550, 11 rue de l'Université, F-67000 Strasbourg, France

⁸ Space Telescope Science Institute, 3700 San Martin Drive, Baltimore, MD 21218, USA

⁹ UCO/Lick Observatory, University of California, 1156 High Street, Santa Cruz, CA 95064, USA

¹⁰ Department of Physics, Anhui Normal University, Wuhu, Anhui, 241000, China

¹¹ School of Astronomy and Astrophysics, Nanjing University, Nanjing, 210093, China

¹² Instituto de Astrofísica e Ciências do Espaço, Universidade de Lisboa, OAL, Tapada da Ajuda, PT1349-018 Lisbon, Portugal

¹³ Departamento de Física, Faculdade de Ciências, Universidade de Lisboa, Edifício C8, Campo Grande, PT1749-016 Lisbon, Portugal

¹⁴ Department of Astronomy and Astrophysics, The Pennsylvania State University, University Park, PA 16802, USA

“missing” black holes are the key to understand the mass build-up of SMBH in the first Gyr of the Universe and to improve our understanding of their formation and early evolution. In fact, the mechanism of SMBH formation is still a matter of debate since their growth up to $\sim 10^9 M_\odot$ by $z \sim 7$ (Mortlock et al. 2011) cannot be explained by Eddington limited accretion onto ordinary stellar remnant seed black holes in such a short time. This *problem* can be solved by invoking the formation of massive BH seeds at $z \geq 10$ or supercritical accretion episodes (Madau et al. 2014).

Theorists are debating if the SMBH seeds were formed by the collapse of an early generation of stars (named Population III, POPIII) or from the direct collapse of pristine gas clouds (Direct Collapse Black Holes, DCBHs). The end point of the evolution of a POPIII star is a $\sim 10^{1-2} M_\odot$ BH, while DCBH can easily reach $\sim 10^{5-6} M_\odot$ already at $z \geq 10$ (Yue et al. 2013). Volonteri (2010) predicts that, if the main SMBH seeding mechanism was DCBH, then the number density of low luminosity AGN should rapidly decline at $z \geq 3$, while if the seeding mechanism was mainly due to POPIII stars then the number density of low luminosity AGN at $z \geq 3$ should decline more gently. Unfortunately there are no direct observational evidences of SMBH seeds, though indirect arguments based on the X-ray and near-IR backgrounds (see e.g. Kashlinsky et al. 2012; Cappelluti et al. 2013; Yue et al. 2013) or stacking (Treister et al. 2013) suggest that significant progresses may be obtained by a synergic multi-wavelength approach.

By combining *Chandra* 2 Ms deep X-ray observations (Luo et al. 2008) and optical/ near-infrared images in the z,K,IRAC images in the GOODS-MUSIC field along with F160W data in the ERS (Early Release Science, Grazian et al. 2011) region Fiore et al. (2012) pushed the formal detection limits of the X-ray images at deeper levels using the optical near infrared images as priors. Giallongo et al. (2015) improved the method outlined above using 4 Ms *Chandra* data and F160W GOODS images. The optical/near infrared priors have then been used to select high redshift ($z > 4$) AGN and evaluate their impact on the reionization history of the Universe (Giallongo et al. 2015). Pushing the limits of deep *Chandra* Surveys towards ultra faint fluxes would also allow to boost the detections of faint (Lehmer et al. 2012) *normal* (SFG) galaxies which start to outnumber AGN around $10^{-17} \text{ erg cm}^{-2} \text{ s}^{-1}$ in the 0.5–2 keV band. The detection of additional very faint X-ray sources and their identification in the optical/NIR may lead to the discovery of moderate redshift ($z \sim 1-2$) SFG and improve the current knowledge of the cosmic evolution of binaries in galaxies. The evolution of SFGs has been mostly determined via stacking of optically selected samples (Basu-Zych et al. 2013). Stacking is a powerful tool, however the outcomes of these investigations are strongly influenced by the choice of the reference sample. Samples of X-ray detected SFGs are available only up to $z \sim 1.3$ (Mineo et al. 2014) making it difficult to perform a direct determination of their evolution around and beyond the peak of cosmic star formation at $z \sim 2-3$. In order to increase these sample sizes we need to boost our efficiency in detecting faint sources by developing new source detection

techniques.

Unfortunately, the sky area sensitive to extremely faint fluxes (and luminosities) is very small and therefore only a handful of faint sources (either high- z AGN or SFG) have been detected so far. While we cannot push the flux limit to fainter fluxes, we can develop methods that allow us to increase the efficiency of source detections.

The method described in this paper is conceptually similar to that followed by Giallongo et al. (2015) and originally proposed in Fiore et al. (2012), but differs from standard methods usually adopted in the literature. The most recent and comprehensive discussion is reported in Hsu et al. (2014) where the optical/NIR counterparts are searched within the X-ray positional error box. The here proposed method maximizes the number of CANDELS sources with an X-ray counterpart. The advantage here is that, thanks to the unprecedented depth of WFC3 images (down to $m_{AB} \sim 29-30$ in H-band), almost the totality of the counterparts of the X-ray sources are already detected in the CANDELS H-band catalogue. In fact the likelihood that a *Chandra* source has a counterpart with H magnitude below the detection limit of WFC-3 is very low. Moreover, in this paper we take advantage of the superb *Chandra* angular resolution and astrometric accuracy, that guarantees the capability of associating a very large fraction of X-ray sources to optical/NIR counterparts in HST images (Xue et al. 2011; Civano et al. 2012; Hsu et al. 2014). As mentioned above a well established method in the literature, is to assign a counterpart to the X-ray detection with the Likelihood Ratio (LR) technique (see e.g. Ciliegi et al. 2005; Brusa et al. 2007; Civano et al. 2012). Here we employ the LR technique to evaluate the reliability of our source detection, counterpart assignment and to complement our catalog in the few cases where our method fails. Other authors used a similar approach but validating the associations with a bayesian analysis (e.g. Hsu et al. 2014). The CDFS/GOODS-S was observed by HST-WFC3/ACS in the Cosmic Assembly Near-Infrared Extragalactic Legacy Survey (CANDELS) which incorporates a wide 0.048 deg^2 observation plus the so-called Hubble Ultradeep Field (UDF) and, thanks to the extraordinary sensitivity, reaches H-Band depth of $m_{AB} \simeq 28$ (Guo et al. 2013).

The outstanding quality of the HST CANDELS catalog, combined with the sub-arcsec angular *Chandra* resolution, makes it possible to directly perform a PSF fitting of X-ray data at the position of each HST source.

The overall approach is similar to that pioneered by Fiore et al. (2012), but it benefits of improved detection techniques and homogeneous treatment of the data as well as of extensive simulations. Even though, at the time of writing, a large fraction of the ultradeep 7 Ms *Chandra* observations in the CDFS were performed, we here rely on the 4 Ms dataset (Xue et al. 2011, hereafter X11), with a flux-limit $S_{lim} \sim 10^{-17} \text{ erg s}^{-1} \text{ cm}^{-2}$ in the 0.5-2 keV (i.e. $\log(L)=42.6 \text{ erg/s}$ @ $z=6$), since it allows a more robust comparison with published data. The additional observations in the CDFS are used as a posteriori test.

Throughout the paper we adopt a concordance Λ -CDM cosmology with $\Omega_\Lambda=0.7$, $\Omega_m=0.3$ and $H_0=70 \text{ h}_{70}^{-1} \text{ km s}^{-1} \text{ Mpc}^{-1}$. Unless otherwise stated, errors are quoted at the 1σ level.

2. OBSERVATIONS AND DATA ANALYSIS

The 4Ms CDFS consists of 23 observations described in Table 1 of Luo et al. (2008) plus other 31 pointings described in X11 for a total exposure of ~ 4 Ms. For the purpose of this paper we employed only observations taken with a focal temperature of ≤ 120 °C since at higher T the background cannot be modeled with our technique (see below). Differently from Luo et al. (2008) and X11, because of higher detector temperature, we discarded *Chandra* OBS-ID 1431/0-1 ending up with a total exposure time of ~ 3.8 Ms.

For every pointing, level 1 data were reprocessed using the *chandra_repro* software in CIAO and CALDB 4.6.1 released by the *Chandra* team. Spurious signals from cosmic rays and instrumental features have been removed as well as time intervals with flaring particle background. After cleaning, the effective exposure time is ~ 3.6 Ms. Astrometry has been improved by matching a high significance X-ray source catalog with the Guo et al. (2013) catalog in the H magnitude range $15 < m_{AB} < 23$. Images were created in the [0.5-2] and [2-7] keV energy bands, respectively. In the same bands we created exposure maps at effective energies of 1.2 and 3.2 keV, respectively. Both images and exposure maps have a bin size of $0.5''$. In the same energy bands we created background maps by using the CXC blank fields library. Above 9.5 keV the mirror effective area of *Chandra* is basically zero; this means that the events accumulated at those energies are due to non cosmic (particle) interactions with the detector and the satellite. The level of the non cosmic flux is variable because of several factors (e.g. Solar activity) but its spectral shape is constant in time (Hickox & Markevitch 2006). Thus, in order to obtain a realistic particle background it is sufficient to rescale the maps in any band by the ratio of the [9.5-12] keV number of events in the templates to the [9.5-12] keV number of events in the real event file (see below for a more detailed treatment).

While precise in estimating the particle background, this method may introduce a bias in the determination of the level of purely cosmic diffuse background. Blank field event files contain a certain level of galactic background. In fact, by construction blank field files are produced by averaging source-removed event files of extragalactic fields and randomizing the position of remaining photons in order to remove background fluctuations clustering features (Cappelluti et al. 2012). The CDFS is a high latitude field and its background is well approximated in the blank field file library. However since we assume that the particle background is well modeled by the method above described, the level of galactic and solar system CXB could be over- or underestimated. For that reason, after masking for X11 detected sources, we computed the following quantity

$$\Delta_{CXB}(E, d) = \sum_N(E, d) - \sum_N(E, b) \quad (1)$$

where $\sum_N(E, d)$ and $\sum_N(E, b)$ are the total number of CXB photons in the energy band E in the data and in the blank field files in any given pointing, respectively. This quantity, scaled to account for the source's masked area, is the number of over- or underestimated local CXB photons in our maps. The Δ_{CXB} photons are then redistributed across the field of view and the detector accord-

ing to the energy dependent exposure map. In this way we expect a good agreement between the real and the modeled background. A full description of the method can be found in Hickox & Markevitch (2006). The images created with this method suffer from Poisson random noise and cannot be adopted as background models. For these reasons the assembled mosaic of background maps have been smoothed by using a Gaussian filter with $\sigma = 20''$.

3. SOURCE DETECTION WITH *CMLDETECT*

Here we briefly summarize our source detection method and the main features of the detection software. We employed a modified version of the XMM-SAS tool *emldetect*. A description of the algorithm and of the statistical theory behind it can be found in Cruddace et al. (1988). While several authors have used *cmldetect* for analyzing *Chandra* surveys (see e.g., Puccetti et al. 2009; Krumpke et al. 2015), the major step forward here is the employment of WFC3-HST galaxies as priors to improve the efficiency on faint sources and to facilitate the identification process.

This code has been initially developed for ROSAT and XMM-Newton, and it was adapted (Puccetti et al. 2009; Krumpke et al. 2015) for use with *Chandra* with a customized version of the software *cmldetect* which makes use of a *Chandra* PSF-Library and the XMM-SAS infrastructure. Unlike the XMM-Newton PSF, the *Chandra*-PSF does not depend exclusively on energy and off-axis angle, but also on the azimuthal position. Such a feature cannot be handled by the XMM-SAS infrastructure; thus, in order to allow the software to work with *Chandra*, we created an *ad-hoc* PSF library by averaging over all the azimuthal angles the PSF templates in energy and off-axis angle bins. This approximation has been proved to be effective on several Monte Carlo simulations and on real data within the *Chandra* COSMOS survey (Puccetti et al. 2009). Moreover, since the geometry of the 4Ms CDFS mosaic is such that the roll angles are basically random, in this way the azimuthal PSF dependence is smeared out and the approximation adopted in our PSF library carefully represents the real data.

Given an input list of source positions, simultaneous maximum likelihood PSF fits to the events distribution on the detector are performed in all energy bands at the same time. Since the *Chandra*-CDFS 4 Ms observations have aimpoints separated by $< 1'$, we employ the cumulative mosaic image and we fixed as a reference optical axis the mean pointing position at $\alpha = 03^h 32^m 28^s.06$, $\delta = -27^\circ 48' 26''$.

The most important fit parameters are: the source location, source extent (beta model core radius), and source count rates. Sources with overlapping PSFs are fitted simultaneously. The maximum allowed number of sources that can be fitted simultaneously is limited to 10, and it is ruled by the parameter *nmaxfit* which sets the maximum number of sources which are considered simultaneously. After some trial, we set *nmaxfit* = 5 as a compromise between the deblending performances and the computational times, that become impracticable for larger values.

Two parameters determine the image region on which a source fit is performed: *ecut* determines the size of the sub-image around each source used for fitting, and *scut*

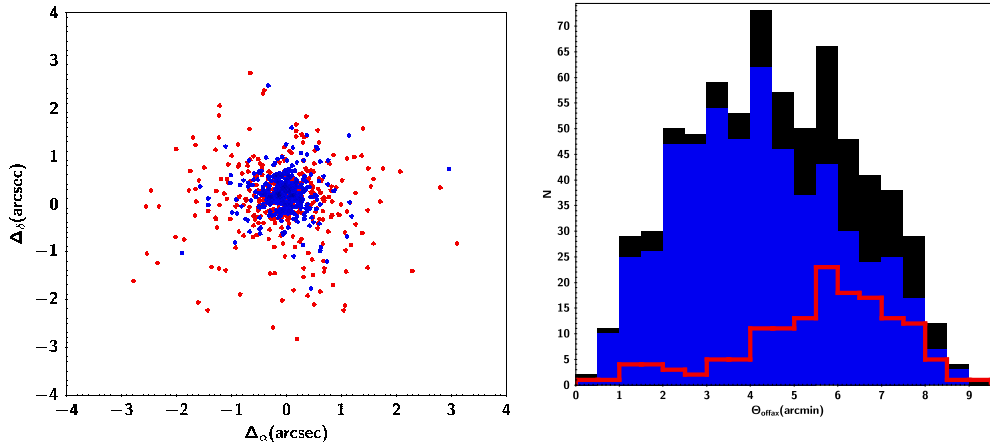


FIG. 1.— Left: The separation between the input position and the best fit X-ray centroid in arcsec In red for sources with $\mathcal{L} < 10$ and in blue for those with $\mathcal{L} \geq 10$. Right: the offaxis angle distribution of the sources with an input vs output position smaller (blue filled histogram) and larger (red histogram) than $1''$ compared to that of the whole sample (black filled histogram).

determines the radius around each source, in which other input sources are considered for multi-PSF fitting. Both *ecut* and *scut* are given as encircled energy fractions of the calibration PSF. For our purposes we fixed *ecut*=0.68 *scut*=0.9 as in Puccetti et al. (2009).

All detection likelihoods are transformed to equivalent likelihoods \mathcal{L}_2 (\mathcal{L}) (see XMM *emldetect* manual¹⁵), corresponding to the case of two free parameters to allow comparison between detection runs with different numbers of free parameters:

$$\mathcal{L}_2 = -\ln(1 - P(\frac{\nu}{2}, \mathcal{L}')) \quad \text{with} \quad \mathcal{L}' = \sum_{i=1}^n \mathcal{L}_i$$

where P is the incomplete Gamma function, n is the number of energy bands involved, ν is the number of degrees of freedom of the fit ($\nu = 3 + n$ if task parameter *fitextent*=yes¹⁶, and $\nu = 2 + n$ otherwise), and $\mathcal{L}_i = C_i/2$ where C is the statistics defined by Cash (1979). The equivalent detection likelihoods obey the simple relationship

$$\mathcal{L}_2 = -\ln(p), \quad (2)$$

where p is the probability for a random Poissonian fluctuation to have caused the observed source counts. Note that for very small numbers of source counts (less than ≈ 9 counts, Cash 1979), this relation likely does not hold and thus the low count regime must be tested with *ad-hoc* simulations.

For this work, the input list for *cmldetect* was made by the positions of the 34930 CANDELS GOOD-S WFC-3 selected sources (Guo et al. 2013) on a total area of 0.048 deg^2 . The details of the parameters adopted and the properties of the resulting catalogs are described later in Sect. 5. Here we focus on the detection process and the association with the input priors.

As a first step, we fixed the source position (parameter *fitposition*=no in *cmldetect*) to the input value, while the source flux was the only free parameter. The fit

was performed in the [0.5-2] keV and [2-7] keV energy bands simultaneously. Thus, by construction the equivalent likelihood from which we set the threshold is that of the [0.5-7] keV band. For our purposes we did not search for extended sources, thus we set *fitextent*=no. We first apply a preliminary threshold at $\mathcal{L}_2 \geq 3$ while the final threshold for the catalog is chosen only after the simulations (see below). Due to PSF blurring bright sources are observed on several pixels, especially off-axis, the same X-ray source could be the counterparts of several CANDELS galaxies. If there are more than 5 candidates with our Multi-PSF fitting software it could happen that at the location of bright sources and on their PSF wings the software could find more detections. If the source is detected with more than 400 counts (i.e. $<10\%$ of all the sources in the 4Ms CDFS, see below), within the 90% of the PSF radius we keep only the detection with the higher \mathcal{L} and remove the other(s) from the catalog. At lower counts levels a visual inspection does not show any obvious case of multiple sources.

Although the astrometry of *Chandra* is calibrated to be precise within $0.5''$, offsets between the X-ray and the near-IR position may exist, and lead to additional errors in the determination of the X-ray flux. To verify this effect and to provide the best possible coordinates for the X-ray centroid we then released the constraints on the position of the X-ray emission by letting *cmldetect* run with *fitposition*=yes. In doing so we realized that the internal structure of *cmldetect* software loses track of the actual ID of the prior during the multi source fit within the PSF encircled energy fraction parameters set by *scut* and *ecut*. Since this is a crucial information we had to correct for this effects *a-posteriori* so, by inquiring the software developer¹⁷ and after testing the procedure, we assigned again the source to the prior that is closer to the X-ray centroid. This is not meant to assign a counterpart to the X-ray source, but simply to keep track of the input prior source. However, we have also found that in some case the revised position of the X-ray centroid is significantly shifted with respect to the position of the original prior. This is shown in Fig. 1, where we show the displacement between the best fit

¹⁵ <http://www.cosmos.esa.int/web/xmm-newton/sas>

¹⁶ If *fitextent*=yes the sources are also fitted with a convolution of beta or gaussian profiles with the PSF and if the likelihood obtained is significantly larger than that obtained with the PSF only, the source is classified as extended

¹⁷ H. Brunner personal communication

and input CANDELS sources position. We note that for $\sim 80\%$ of the sources the X-ray centroid is consistent with the position of the input source within $1''$, although there is however a tail at larger offsets (i.e. $\simeq 20\%$ at $> 1.0''$ and $< 10\%$ at $> 1.5''$).

This effect depends strongly on two quantities: the position on the field and the X-ray intensity. Indeed, as one can notice in the right panel of Fig. 1, the majority of the sources with large offset are objects detected at low significance ($\mathcal{L} < 10$) and at off-axis angles $> 4.5'$ (see Fig. 1).

This is not entirely surprising - it is well known that the image quality of the Chandra images on the Goods-South field degrades significantly at large offset from the center, most notably due to a significant degradation of the PSF, that leads to a lower positional accuracy. It also indicates that the centering of X-ray sources becomes difficult at low S/N .

To investigate the origin of this shift we have visually inspected all the relatively few ($\simeq 30$) sources that have an offset larger than $1''$ but are also detected at good S/N (i.e. $\mathcal{L} > 10$), i.e. those for which the X ray position can be determined unambiguously. We have verified that in most cases the large shift is due to some error in the determination of the X-ray centroid, usually due to the poor PSF at wide distances from the center (most of these sources are indeed close to the image edges) or to tensions between the position in the soft-X and hard-X images. In nearly all cases however the association with the optical prior is robust, since the true X-ray center is actually close to the optical center. However, at this stage of the analysis, the association of a prior to a X-ray source should not be considered as an identification but simply as a test of the robustness of the procedure.

To better scrutiny the reliability of our procedure and the origin of possible systematic effects we have designed a set of simulations and a comparison with other approaches to source detection, that are described in the following sections.

4. CANDELS X-RAY SIMULATIONS

The production of a source catalog requires a deep knowledge of its statistical properties as well as its limitations. In particular a fundamental property of a catalog is the selection function and the contamination from spurious detections. The best way to evaluate these characteristics is to test the procedure on a sample of simulated source whose properties are known *a priori*. Also the instrument simulating carefully the property of the instrument is fundamental to evaluate the quality of the catalog. In this section we present the statistical properties of our catalog as well as validation of the quality of the method.

4.1. Simulated galaxies and AGN samples.

Detecting X-ray sources using Optical/NIR priors is a relatively new procedure (see e.g. Fiore et al. 2012) which needs specifically designed simulations to validate its photometric accuracy and source detection yield. Every CANDELS galaxy was assigned an X-ray flux and folded into a ray-tracing MARX (Model of AXAF Response to X-rays) simulation to mimic the *Chandra* performances. In order to reproduce in a realistic way our

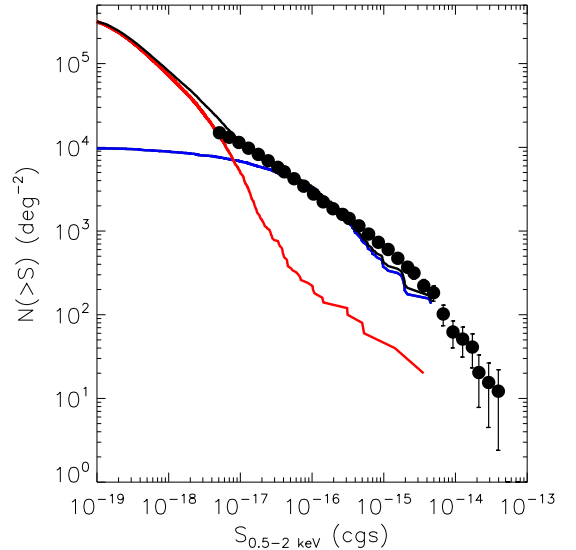


Fig. 2.— Comparison of the simulated [0.5-2] keV cumulative number counts $\log N\text{-}\log S$ for SFGs (*red continuous line*) and AGN (*blue continuous line*) with the measurements of Lehmer et al. (2012) in the CDFS (*black filled circles*). The total model SFG+AGN is plotted as a *black continuous line*.

mock sample we created artificial X-ray fluxes of CANDELS galaxies from the estimated $L_{8-1000\mu m}$ by using *ad-hoc* scaling relations between L_{IR} and L_X (see below). Infrared luminosities (L_{IR} , from 8 to $1000\mu m$) are predicted for all galaxies in the catalog starting from their observed photometric redshift, their stellar mass (Santini et al. 2014), their *UVJ* rest-frame colors and their observed (or extrapolated from the SED) UV luminosity (1500\AA). We first split our sample into actively star-forming and quiescent galaxies using the *UVJ* color-color selection (Williams et al. 2009). Quiescent galaxies are given zero L_{IR} . For star-forming galaxies, we predict their total SFR assuming that they follow the redshift dependent $SFR\text{-}M_*$ correlation, the so-called “main sequence” of star-forming galaxies, using the observed relation from Schreiber et al. (2015) and adding a 0.3 dex random scatter, mimicking the observed dispersion of the $SFR\text{-}M_*$ correlation. We convert the rest-frame UV luminosity into a non-obscured SFR using the formula introduced in Daddi et al. (2004), and subtract it from the predicted SFR to recover only the dust-obscured component. Finally, we convert this remaining SFR into L_{IR} using the formula of Kennicutt (1998). In order to derive the X-ray luminosity of Galaxies we adopted the prescription of Basu-Zych (2013) which relates z and SFR to L_X for star-forming-galaxies. Galaxies with a predicted [0.5-2] keV flux $< 10^{-20}$ (cgs) were flagged with $S_X=0$.

A fraction of CANDELS galaxies could be AGN which are powerful X-ray sources. In order to include AGN X-ray emission in our sample, we divided the sample in $\Delta(z)=0.1$ redshift bins, and in every bin we assigned an AGN flux (S_{AGN}) to a fraction of galaxies consistent with that expected by the Gilli et al. (2007) population synthesis model down to $10^{-20}\text{ erg s}^{-1}\text{ cm}^{-2}$. We point out that with this method the luminosity function of X-ray AGN is correctly reproduced, but the random choice of the AGN host galaxy does not allow us to obtain the

correct optical/NIR luminosity distribution of the simulated X-ray source counterparts. As a result, we may typically assign AGNs to galaxies that are fainter than the real AGN hosts.

In Fig. 2 we show the simulated logN-logS of X-ray sources derived with this method compared with the number counts measured by Lehmer et al. (2012).

4.2. Ray-tracing events simulation

To simulate the CANDELS X-ray sources we employed the raytracing software MARX which provides a detailed ray-trace simulation of *Chandra* observations and can generate standard FITS events files and images as output. It reproduces the *Chandra* mirror system and all focal plane detectors, including ACIS-I. The pointing direction, boresight, roll angle and dithering were reproduced to simulate all the 34930 CANDELS sources. Every input source was assigned a photon X-ray spectrum modeled as a simple power-law with $\Gamma=1.4$ plus Galactic absorption with $N_H=7 \times 10^{19} \text{ cm}^{-2}$ (Dickey & Lockman 1990) and a normalization derived from its flux. For every galaxy the software produces the expected number of events as a function of energy by randomly drawing them from their spectral distribution. Every photon has been spread on the detector according to the actual PSF template from calibration at any given energy and radial/azimuthal coordinates. Detector response was reproduced within MARX, pixel randomization was also applied. Dithering of the satellite was also taken into account by using an internal MARX model. Since the software can handle one source and one pointing per run, for every galaxy we produced 54 event files. All the 34930 sources event files simulated over 54 pointings were co-added and reprojected to the same tangent point. For every pointing, the background in the energy band [E] has been estimated with the technique described by Hickox & Markevitch (2006) by randomly extracting events from the blank field background files so that $B_{sim}[E] = \frac{B_d[9.5-12]}{B_m[9.5-12]} B_m[E]$ where, $B_{sim}[E]$, is the number of background events in the energy band [E], $B_d[9.5-12]$ is the number of events in the real data in the [9.5-12] keV energy band, $B_m[9.5-12]$ is the number of events in the blank field event files in the [9.5-12] keV energy band and $B_m[E]$ is the number of events in the blank field event files in [E] energy bands, respectively. The sources and the background simulations were then merged in a single event file and images were produced.

4.3. Method reliability : source detection on simulated maps

We use these simulations to test the detection procedure and to verify its efficiency. Synthetic images were produced from the simulated event files in the [0.5-2] keV, [2-7] keV and [0.5-7] keV energy bands with a spatial binning of $0.5''$. Similarly we used the resampled blank field background maps described in Sect. 4.2 to create background maps in the same energy band and with the same spatial binning as in images. Background maps were smoothed with a Gaussian kernel with $\sigma=20''$. As exposure maps we employed those computed for the real data.

We ran a source detection on the simulated images with the same parameters of the real data. In the real data,

in $\sim 20\%$ of the cases, the actual detected source is found more than $1''$ away from the galaxy flagged as prior. By making use of our simulations we checked this fraction and found the same result. We first notice that the values of \mathcal{L} of most of the detected sources improves significantly by fitting of the position (i.e. by using *fitposition=yes* compared to *fitposition=no*). As in the real data, the fraction of sources for which we find a $>1''$ displacement between the prior and the best fit X-ray centroid shows a strong radial dependency. At offaxis angles $<4.5'$, the number of such sources is of the order of 5% while, at larger offaxis angles, this fraction is of the order of 30%. Since the only difference between center and off-center in the simulations is the degraded PSF, we conclude that a larger fraction of the X-ray centroids at relatively large off-axis angles are significantly displaced from their prior due to the PSF degradation.

We can use the simulations to verify the accuracy of our procedure in determining the correct prior. This is not straightforward since in our simulations a X-ray flux is assigned to all the star-forming galaxies in the input sample. Most of them have fluxes very small, definitely below the detection limit, but also non-zero. To take this into account we used the statistical approach used in (Cappelluti et al. 2007), that compares the input and output catalogs of the simulations using the match in both position and flux. We evaluated how many "prior" sources are the actual counterpart of the detected X-ray sources by cross-correlating our output catalog with the input one by minimizing the following quantity (Cappelluti et al. 2007):

$$R^2 = \left(\frac{X_{out} - X_{in}}{\sigma_{X,out}} \right)^2 + \left(\frac{Y_{out} - Y_{in}}{\sigma_{Y,out}} \right)^2 + \left(\frac{S_{out} - S_{in}}{\sigma_{S,out}} \right)^2 \quad (3)$$

where X,Y are the coordinates on the detector and S is the flux in the [0.5-7] keV band, respectively. This estimator is also known as Mahalanobis distance (Johnson et al. 2007). The subscripts *in* and *out* stand for input and output catalogs, respectively. As a first result, we find that for $\sim 2\%$ and $\sim 8\%$ of the detected sources on- and off-axis respectively, the actual counterpart is not the prior.

We also tested the accuracy of the photometry: in Fig. 3 we show the [0.5-2] keV input vs output counts. As in Puccetti et al. (2009) the output/input counts ratio is consistent with 1 and spread according to a Poisson distribution. At faint fluxes the distribution appears to be skewed toward high C_{out}/C_{in} ratios because of a sort of Malmqvist bias" - i.e. we do not plot in Fig. 3 objects with a low \mathcal{L} parameter.

These simulations are able to guide us in the choice of a crucial parameter, namely the detection threshold. At this aim, we have to compute the expected number of background fluctuations detected as sources as a function of the detection likelihood \mathcal{L} . We did this by running a source detection using as X-ray map a randomized image of the modeled background and the CANDELS catalog as input. In this way the number of detections can be considered an estimate of the overall number of spurious detections in the real data. In Fig. 4 we show the cumulative distribution of the ratio between the spurious sources detected in these simulations and the real sources

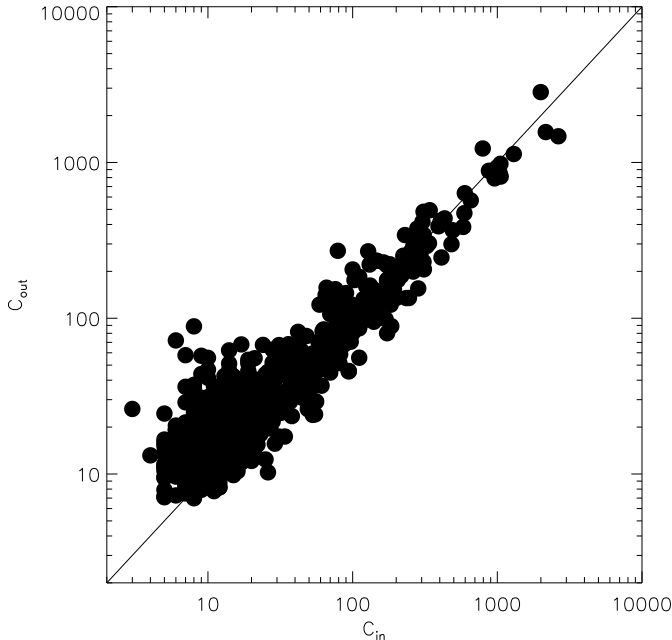


FIG. 3.— Photometry efficiency test on the simulations. The input versus output source counts.

detected in the data as a function of the \mathcal{L} parameter. Since the goal of this paper is to push the limit of deep fields beyond the actual one and maximize the detection of faint sources, we estimate that an acceptable spurious fraction should not be higher than 5%, compared to the usually adopted values of $\sim 1\text{--}2\%$. This fraction corresponds to values $\mathcal{L} > 4.98$ and translates into a minimum flux detection significance of $\sim 2.7\sigma$ (Eq. 2). This is similar to the value reached with blind detections at comparable background levels (Luo et al. 2008; Xue et al. 2011).

Finally, we checked if the simulated background carefully represents the actual level. In fact, we know that the real background fluctuations (Cappelluti et al. 2012) are not randomly distributed, but are strongly correlated. On the other hand the simulated background is relatively smooth and uniform and this could introduce a bias in the spurious fraction estimate. For that reason we performed a source detection on the real data masked for the detected sources according to the PSF size at the source location. The unmasked part of the image can be considered as a fair estimate of the real background. We have then produced a catalog of 34930 positions drawn from the real catalog by randomly placing the artificial sources in an annulus with inner and outer radii $5''\text{--}10''$ from the real prior sample of sources, respectively. In this way we preserve the spatial distribution of the CANDELS sources in the input catalog but we do not overlap with real sources. We then ran our source detection on this masked image by using as input catalog the random sample above described. We repeated such a procedure 20 times. All these detections are nothing else but random background fluctuations which would enter the catalog as spurious sources. The results found with this test are fully consistent with those obtained with the randomized background images.

We then computed the selection function of our detec-

tion procedure by evaluating the ratio of the number of retrieved input sources with respect to that of input ones in bins of intrinsic input flux of $\Delta \log(S_{in}) = 0.1$. The resulting cumulative histogram is smoothed with a filter width of $\delta \log S = 0.3$. The final sky coverage is shown in Fig. 5. Note that here we present the sky coverage with respect to the intrinsic (and not the detected) flux of the X-ray sources.

The results are compared with those of Lehmer et al. (2012) obtained with a Bayesian method for flux calculation and for blind X-ray source detection in the CDFS. As expected, the faintest recovered sources detected with the two methods have a similar flux, but our method yields a steeper selection function at faint fluxes. As an example, in the $[0.5\text{--}2]$ keV band, with a thresholds $\mathcal{L} > 4.98$ (see below) in the faintest fractions of decade of fluxes our method can recover about a factor 5 more sources. This is particularly evident in $[0.5\text{--}2]$ keV energy band, but not as much in the $[2\text{--}7]$ keV band. This is due to the fact this method take advantage of highest angular resolution of *Chandra* at low energies.

In summary, in this work we have explored the advantages of using a prior-based search for X-ray sources in the GOODS-South field, using the *cmlddetct* software. These evidences allow us to draw the first conclusions about the quality of this method: a) at offaxis angles $< 4'$ for 98% of the sources the prior galaxy is likely to be the counterpart to the X-ray source. b) at offaxis angles $> 4'$ (i.e. if the PSF HEW $> 1.5''$) the prior sources and the relative detected X-ray sources are significantly displaced in 20% of the cases, but for 92% of the sources the prior galaxy is likely to be the counterpart to the X-ray source. c) the source detection quality is improved by fitting in any case the position of the X-ray centroid, c) using a deep optical catalog as a prior, increases the probability to detect a faint X-ray source compared to that of a blind detection based on background fluctuations. To some extent, the limitations in this approach are certainly due to the complex nature of the X-ray data in the CDFS area, that degrade at large distances from the centre. However, some of these limitations can be due to the specific performances of *cmlddetct*, that was not originally designed to be used in this way. In future works we plan to adapt other prior-based software for photometry (like T-PHOT, Merlin et al 2015) to the case of X-ray data.

5. X-RAY CATALOG ASSEMBLY

Armed with the results of the simulations described above, we have obtained the final catalog in the GOODS-South field. We summarize in this section the procedure finally adopted and the comparison with other approaches.

5.1. The prior-based catalog

We run the source detection on the 4 Ms CDFS data $[0.5\text{--}2]$ keV and $[2\text{--}7]$ keV band simultaneously and the likelihood is computed in the $[0.5\text{--}7]$ keV band. We used as input catalog the positions of the 34930 sources detected by Guo et al. (2013) in the CANDELS GOODS-S area and set *fitposition*=no and we imposed a $\mathcal{L}=4.98$ threshold in the resulting $[0.5\text{--}7]$ keV energy band. In this way we preselected 735 sources, some of which corresponding to the same X-ray source. We then fitted the

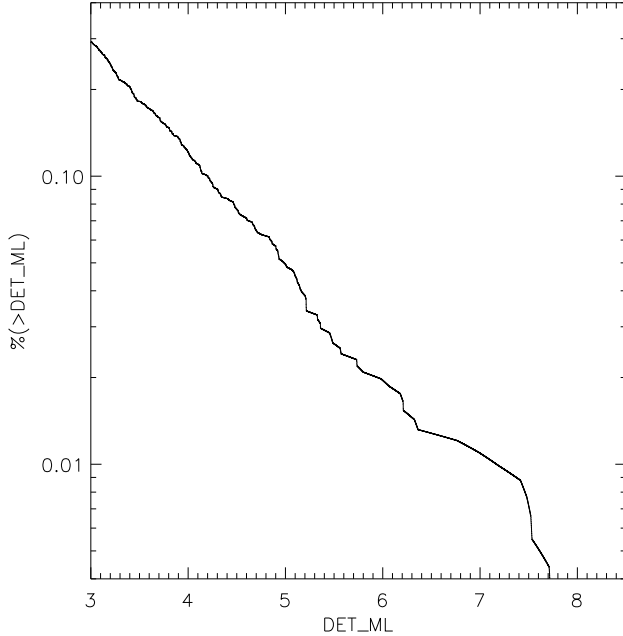


FIG. 4.— The fraction of spurious detections in the GOODS-S field as a function of the detection likelihood as determined by our Monte Carlo simulations in the [0.5-7] keV band.

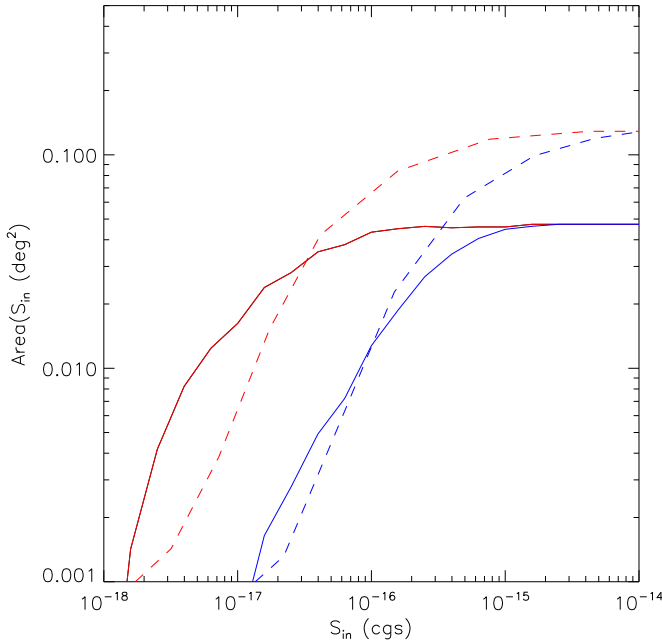


FIG. 5.— The sky area vs input flux selection function plot for our sample in two sub-bands compared with that of Lehmer et al. (2012). The red – continuous and the blue – continuous line represent the selection functions in the [0.5-2] keV and [2-7] keV energy bands, respectively. The red – dashed and the blue – dashed line represent the selection functions from Lehmer et al. (2012) in the [0.5-2] keV and [2-7] keV energy bands, respectively. Hard band fluxes have been extrapolated to [2-10] keV fluxes

position of the sources to determine the best possible X-ray centroid of each detected source. At this threshold we detect 698 unique sources, in the ~ 0.048 deg² of the

TABLE 1
NUMBER OF DETECTIONS

	[0.5-2] keV	[2-7] keV	[0.5-7] keV
$N(\mathcal{L} \geq 4.98)$	531	285	698
$n(\mathcal{L} \geq 4.98)$	352	106	61
$N(X11)$	466	254	527
$N(X11+C15)$	*	*	784
S_{lim}	0.11	0.87	0.89

NOTE. — From top to bottom: $N(\mathcal{L} \geq 4.98)$ is the actual number of significant detections in the three energy bands; $n(\mathcal{L} \geq 4.98)$ is the number of sources significantly detected in a given energy band only (plus full band); $N(X11)$ is the number of X11 significant detections in the three energy bands; $N(X11 + C15)$ is the total number of unique X-ray sources detected in the CANDELS GOODS-S area by X11 and in this work; S_{lim} is the flux limit in each band in units of $\times 10^{-16}$ erg cm⁻² s⁻¹.

CANDELS GOOD-S area analyzed by Guo et al. (2013). We considered only point sources and we did not fit the extension of the sources. Source falling within the region of groups/clusters detected by Finoguenov et al. (2015) were visually inspected individually. For every source, we determine the source counts and the count-rate as an output of the detection algorithm, the background level, the PSF 90% Encircled Energy Fraction (EEF) and the \mathcal{L} in the [0.5-2] keV, [2-7] keV and [0.5-7] keV energy bands, respectively. Count rates were converted into fluxes by assuming a simple power-law spectrum with $\Gamma=1.4$ plus a Galactic absorption $N_H = 7 \times 10^{19}$ cm⁻² (Dickey & Lockman 1990). The Energy Conversion Factors (ECFs) were computed with the online tool *Chandra* PIMMS. The response of the ACIS-I detector varied significantly across the *Chandra* lifetime, for this reason we computed the ECFs for every pointing's epoch and then weight-averaged them according to the exposure time. As a result we obtained a count-rate to flux ECF of 5.32×10^{-12} erg cm⁻² in the [0.5-2] keV band and 2.71×10^{-12} erg cm⁻² to convert the [2-7] keV count-rate into a [2-10] keV flux. The full band count-rate, counts and fluxes are the sum of those in the two sub-bands, respectively. As mentioned above the overall significance of the detection is measured with the cumulative [0.5-7] keV energy band net counts, thus for some sources the parameters in the [0.5-2] keV, [2-7] keV sub-bands may not be accurate. For this reason the flux of the sources for which the sub-band detection has a significance lower than the threshold ($\mathcal{L} < 4.98$), in the specific sub-band should be used with care. While all the sources have $\mathcal{L} \geq 4.98$ in the [0.5-7] keV band, we report 534 and 285 significant detections in the [0.5-2] keV and [2-7] keV energy bands, respectively. We define these sources as $N(\mathcal{L} \geq 4.98)$ in Tab. 1. Among these 352 sources are detected in the [0.5-2] keV but not in the [2-7] keV band, 106 sources in the [2-7] keV but not in the [0.5-2] keV and only 61 sources have a significant detection in the [0.5-7] keV energy band and no significant counterpart in the sub-bands $N(\mathcal{L} \geq 4.98)$. In Table 1 we briefly summarize the properties of the X-ray catalog presented here.

5.2. The comparison with previous catalogs

In the same area X11 detected 527 X-ray sources by using the same X-ray dataset. They used a purely blind X-ray detection without prior knowledge of the actual counterparts. Among these 466, 254 and 527 are detected in the [0.5-2] keV, [2-7] keV and [0.5-7] keV band,

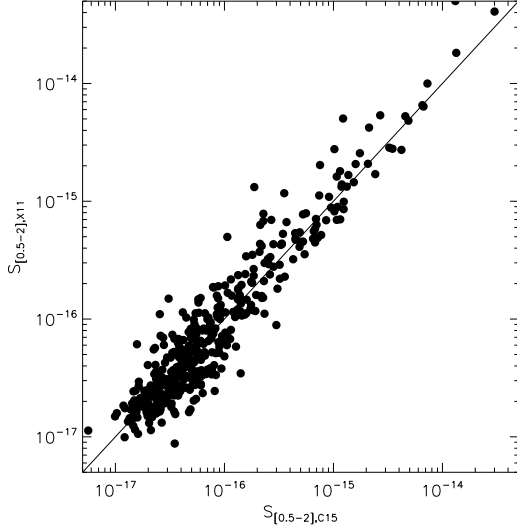


FIG. 6.— The [0.5-2] keV fluxes measured here compared with those of X11 for the common, above threshold sources.

respectively ($N(X11)$ in Tab. 1). A simple positional match between the two catalogs of their catalog with a $2''$ matching radius, returns 443 sources in common, 252 detected with our method only and 85 detected only by X11. In Fig. 9 we show the distribution of the distances between the X-ray centroids found here and those of X11: the average shift is $\sim 0.5''$. By merging our catalog with that of X11 we bring the total number of X-ray detected sources in the CANDELS-GOOD-S area to 784.

As a safety check we cross matched the counterpart catalog of Hsu et al. (2014) with ours for the 443 sources in common with X11. If we consider all the sources with a secure association in our catalog, we find the same association in 90% of the cases. Three quarter of the remaining have an offaxis angle $> 4'$. The likely reason of this discrepancy can be the different method used for the X-ray centroid estimate with our method and the completely different method adapted by Hsu et al. (2014) for assigning the counterpart to the X-ray sources. We compared the fluxes properties of the 443 sources in common with those presented by X11. In Fig. 6 we show the comparison of the [0.5-2] keV fluxes measured by us and those of X11. There is a very good agreement between the measurements and the mean of the ratio of the two measurements is ~ 0.98 . Our count-rate to flux conversion (that uses a fixed spectral slope) is different from that of X11, who use for each source a spectral index obtained from the hardness ratio. This leads to an intrinsic dispersion in the two measurements that has no a clear trend with flux.

We also checked the 85 sources detected by X11 only. Among them 62 have been detected by our software, but with $3.00 < \mathcal{L} < 4.98$ and thus did not satisfy the selection criterion for being included in the catalog. The remaining 28 unmatched sources are all at the very faint limit of their catalog. Therefore 28/571 X11 sources are not found with our method even at $\mathcal{L} > 3$. We can explain this small fraction of “missed” sources with statistical fluctuations among the two catalogs or, alternatively they could belong to the sample of extended sources (see e.g. Finoguenov et al. 2015).

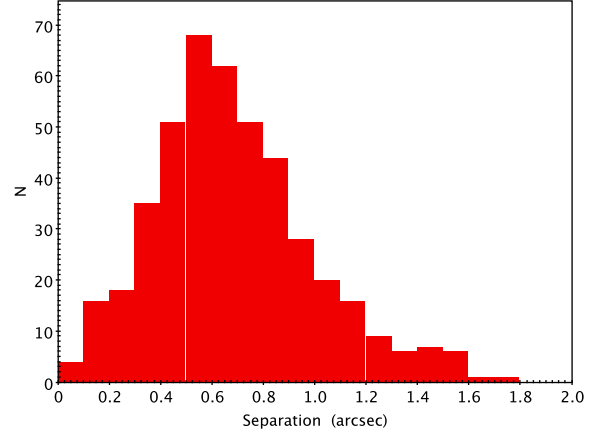


FIG. 7.— Angular separation between the 443 sources in common with the catalog of X11

We also performed a visual inspection of the newly detected sources in this paper with the public deeper observations in the CDFS. At the time of writing ~ 5.9 Ms of data are available in the archive. Among the 698 sources detected in this work only a handful of very faint objects seem to be undetected by visual inspection. Their number is consistent with the expected spurious fraction (5%).

5.3. Validation of the prior matching

As we have shown above, our method potentially suffer from some uncertainties, as shown by the relatively large fraction of objects that are detected at large distances from the priors, especially for faint sources at off-axis angle $> 4'$. According to our simulations a fraction of the detected X-ray sources may not be associated to the input prior at large off-axis angles.

It is therefore interesting to explore the more traditional technique for identifying counterparts of X-ray sources without priors, namely the likelihood ratio technique of Sutherland & Saunders (1992). We followed the procedure of Brusa et al. (2005, 2007) adapted for *Chandra* by Civano et al. (2012). For a given candidate counterpart with magnitude m at a distance r from the X-ray source, the likelihood ratio LR is defined as the ratio between the probability that the source is the correct identification and the corresponding probability for a background, unrelated object $LR = \frac{q(m)f(r)}{n(m)}$, where $q(m)$ is the expected magnitude m distribution function of the real optical counterpart candidates, $f(r)$ is a two-dimensional Gaussian probability distribution function of the positional errors, and $n(m)$ is the surface density of background objects with magnitude m . The distribution of the local background objects, $n(m)$, was computed from each of the three input catalogs using the objects within a $5''$ – $10''$ annulus around each X-ray source. We chose a $5''$ inner radius in order to avoid the presence of true counterparts in the background distribution, and a $10''$ outer radius to exclude the counterparts of other nearby X-ray sources.

The function $q(m)$ has been estimated from our data as follows. We first computed $q'(m) = [\text{number of sources with magnitude } m \text{ within } 3''] - [\text{expected number of back-}]$

ground sources with magnitude m in a $3''$ circle]. The choice of a $3''$ radius is dictated by the requirement of maximizing the statistical significance of the overdensity around the X-ray sources. A smaller radius would include in the analysis only a fraction of the true identifications and the $q(m)$ distribution would be more affected by Poissonian noise. A larger radius would increase the number of background sources.

As extensively described in Brusa et al. (2007), with this procedure $q(m)$ is underestimated at faint magnitudes. At fainter magnitudes, the number density of CANDELS sources within the search radius of each X-ray source is artificially smaller than that expected from the whole sample $n(m)$. The reason for this biased estimate is the presence of a large number of moderately bright CANDELS counterparts within the X-ray centroids. These sources could occupy a non-negligible fraction of the X-ray counterpart search area, making difficult to detect faint background objects. Such a bias would produce an unrealistic negative $q(m)$, which would prevent us from using the LR procedure at faint magnitudes. In order to correctly estimate $n(m)$ at faint magnitudes, we have randomly extracted from the CANDELS catalog 1500 NIR sources with the same expected magnitude distribution of the X-ray source counterparts. Then we computed the background surface density around these random sample of galaxies. Indeed, we found that the $n(m)$ computed in this way is consistent with the first measured $n(m)$ at $F160W < 24.5$ and much smaller than it at faint magnitudes. Therefore, the input $n(m)$ in the likelihood procedure was the global one for $F160W < 24.5$ and that derived with this analysis for $F160W > 24.5$. This allowed us to associate several very faint counterparts to X-ray sources that would have been missed without this adjustment to the procedure. In Figure 8, we show the observed magnitude distribution of the objects in the $1.6 \mu m$ catalog within a radius of $3''$ around each X-ray source (solid histogram), plotted together with the expected distributions of background objects in the same area (red solid histogram). The smoothed difference between these two distributions is the expected distribution of the counterparts ($q'(m)$, black curve) before normalization. The $q(m)$ is obtained by normalizing $q'(m)$ to 1.

For the probability distribution of positional errors, $f(r)$, we adopted a Gaussian distribution with standard deviation, $\sigma = \sqrt{\sigma_{opt}^2 + \sigma_X^2}$, where σ_{opt} is the positional uncertainty for the optical sources that we assumed to be $0.1''$ for all the sources. σ_X was set to $RADEC_ERR$ which is the error in the centroid provided by *cmldetect*. The $RADEC_ERR$ in our catalog spans from $\sim 0.1''$ to $\sim 1.5''$. We also added a $0.25''$ systematic (half *Chandra* pixel) to take into account pixelation effects. Having determined the values of $q(m)$, $f(r)$, and $n(m)$, we computed the LR value for all the sources within $3''$ of the 698 X-ray centroids. As in Civano et al. (2012) and Brusa et al. (2005) we had to choose the best likelihood threshold value (L_{th}) for LR to discriminate between spurious and real identifications. L_{th} must be small enough to avoid missing too many real identifications, so that the completeness of the sample is high and large enough to keep the number of spurious identifications low and increase the identification reliability. Extensive simulations in-

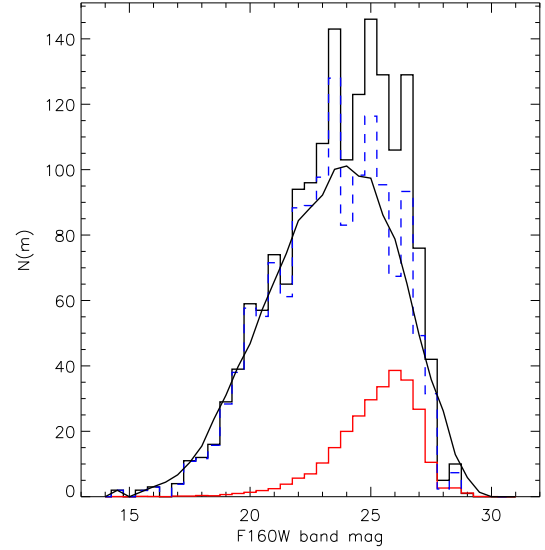


FIG. 8.— *Top*: Black solid histogram the magnitude distribution of all the Guo et al. (2013) sources within $3''$ from our X-ray centroids. Red solid histogram: the expected background magnitude distribution of sources in an annulus with inner radius of $5''$ and outer radius of $10''$ from the X-ray source. The blue dashed histogram is the resulting, non normalized, $q'(m)$ distribution adopted to compute the LR. The Black continuous line is the adopted $q(m)$.

dicate that the trade-off is obtained for $R = C \sim 0.89$ corresponding to $L_{th} = 0.75$. As a result 698 sources have at least a counterpart within the search radius, but only for 608 the association passes the LR test. With this threshold 529 X-ray sources have 1 significant counterpart with $LR > L_{th}$, 74 have 2 and 9 have 3 counterparts, respectively. For 90 sources we do not have a significant counterpart association and they are flagged with $FLAG_ASSOC=2$ in the catalog. However, in many cases, having multiple counterparts does not imply that the identification is unsecure. In order to resolve multiple associations, we computed the distribution of the LR among the possible counterparts of the same X-ray source (Civano et al. 2012).

If such a ratio is larger than the median (LR_{max}/LR_i) then we define the association as secure. In other cases the association is flagged ($FLAG_ASSOC=-1$) as ambiguous and the CANDELS ID number of all the candidate counterparts is listed in the catalog in LR order. Secure identifications are flagged with $FLAG_ASSOC=1$. After this procedure we have 552 secure identifications 57 ambiguous (double to triple) and 89 are unsecure identifications and 3 unidentified (likely spurious X-ray detections). In Table 2 we summarize the results of our identification procedure. As expected, we observe that the fraction of ambiguous and unsecure identifications increases with the offaxis angle.

TABLE 2
THE RESULTS OF OUR LR IDENTIFICATION PROCEDURE.

Class	Number	%
Secure	552	79.1%
Ambiguous	56	8.0%
Unsecure	90	12.9%

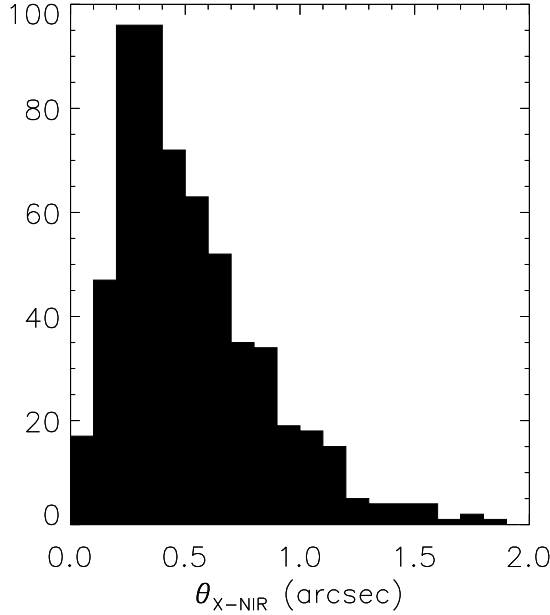


FIG. 9.— The distribution in arcsec of the distances between the X-ray centroid and the optical counterpart for secure identifications.

In Fig. 9 we show the distribution of the distance between the X-ray centroid and the best counterpart in the CANDELS catalog, this distribution peaks at $\sim 0.25''$ and sharply declines down to $2''$.

We can finally compare the results of the prior-based photometry with this likelihood ratio technique. We find that the results are nicely consistent. Indeed, 545/552 ($\sim 98.7\%$) of the secure identifications are associated with the input prior CANDELS ID and 43/57 in the case of ambiguous sources. We note that for this comparison cannot be performed over 90/698 sources, i.e. 13% of the sources, for which the LR does not yield any result.

We point out that the majority of the sources for which the counterpart is flagged as unsecure and is not coincident with prior, are found, on average, with $\mathcal{L} < 10$ and at large off-axis angles and thus with a broad PSF. In particular at off-axis angles $< 4'$ the fraction of sources for which the counterpart is not the prior is $< 1\%$ while at off-axis angles $> 4'$ this is $\sim 9\%$. We added in the catalog a flag, FLAG_PRIOR which has value 1 for off-axis angles $< 4'$ or $\mathcal{L} > 10$ and 2 for off-axis angles $> 4'$ and $\mathcal{L} < 10$. If FLAG_PRIOR=1 one can safely use the prior source as the actual counterparts. Otherwise, one should check if the results of the LR yields to another counterpart. In our simulations the AGN X-ray flux is randomly assigned to a CANDELS Galaxy thus we could not test the LR because the AGN magnitude distribution was the same of that of background sources. If a source with no prior was simulated it would not be detected however, the only source of potential errors is the high probability that a source is detected by chance given a random prior within *ecut*. To evaluate this we performed the following test: to avoid contamination by bright sources we selected 1847 prior candidates within $4''$ of the 500 faintest detected sources. From that catalog we removed the sources which we identified as "BEST_ID" and run the source detection

on 455 of them who have more than one counterpart. We removed a posteriori from the 1847 input sources the actual counterpart of each X-ray source and run the source detection. As a result we have detected only 169/455 detection above threshold with $\mathcal{L} > 4.98$. For these sources the recovered X-ray centroid is consistent with that obtained with the master prior catalog. We repeated the LR test and for 99.5% of the secure matches the best candidate was still BEST_ID. While an evaluation of *ecut* is not straightforward, we notice that the sources not detected by this test are, as expected, those whose prior had a distance from the X-ray centroid larger or similar to *ecut*.

5.4. Catalog columns description

Our catalog is available in machine readable format at the URL <http://www.astrodeep.eu/data/> and on Vizier. Here we describe the columns in the online catalog.

NID: ID of the X-ray source.

PRIOR_ID: CANDELS ID of the optical source used as prior for the X-ray source detection.

FLAG_PRIOR: Flag to determine the reliability of the association with a prior.

BEST_ID: CANDELS ID of the primary optical counterpart of the X-ray source from LR.

SECOND_ID: CANDELS ID of the second best optical counterpart of the X-ray source from LR.

FLAG_ASSOC: Quality of the identification flag.

RA_X: Best fit right ascension in decimal Degree units of the X-ray centroid.

DEC_X: Declination in decimal Degree units of the X-ray centroid.

RADEC_ERR: 1-D error on the X-ray centroid position (arcsec).

SEP: Distance from the best optical counterpart

SCTS_FULL: [0.5-7] keV counts.

SCTS_FULL_ERR: 1σ [0.5-7] keV counts error.

SCTS_SOFT: [0.5-2] keV counts.

SCTS_SOFT_ERR: 1σ [0.5-2] keV counts error.

SCTS_HARD: [2-7] keV counts.

SCTS_HARD_ERR: 1σ [2-7] keV counts error.

\mathcal{L}_{FULL} : $-\ln(p)$ determined in the [0.5-7] keV band.

\mathcal{L}_{SOFT} : $-\ln(p)$ determined in the [0.5-2] keV band.

\mathcal{L}_{HARD} : $-\ln(p)$ determined in the [2-7] keV band.

FLUX_FULL: [0.5-10] keV flux in $\text{erg cm}^{-2} \text{s}^{-1}$ in units 10^{-16} .

FLUX_FULL_ERR 1σ : [0.5-10] keV flux error in $\text{erg cm}^{-2} \text{s}^{-1}$ in units 10^{-16} .

FLUX_SOFT: [0.5-2] keV flux in $\text{erg cm}^{-2} \text{s}^{-1}$ in units 10^{-16} .

FLUX_SOFT_ERR 1σ : [0.5-2] keV flux error in $\text{erg cm}^{-2} \text{s}^{-1}$ in units 10^{-16} .

FLUX_HARD: [2-10] keV flux in $\text{erg cm}^{-2} \text{s}^{-1}$ in units 10^{-16} .

FLUX_HARD_ERR 1σ : [2-10] keV flux error in $\text{erg cm}^{-2} \text{s}^{-1}$ in units 10^{-16} .

RATE_FULL: [0.5-7] keV count rate in $\text{ph cm}^{-2} \text{s}^{-1}$.

RATE_FULL_ERR 1σ : [0.5-7] keV count rate error in $\text{ph cm}^{-2} \text{s}^{-1}$.

RATE_SOFT: [0.5-2] keV count rate in $\text{ph cm}^{-2} \text{s}^{-1}$.

RATE_SOFT_ERR 1σ : [0.5-2] keV count rate error in $\text{ph cm}^{-2} \text{s}^{-1}$.

RATE_HARD: [2-7] keV count rate in $\text{ph cm}^{-2} \text{s}^{-1}$.

RATE_HARD_ERR 1σ : [2-7] keV count rate error in $\text{ph cm}^{-2} \text{s}^{-1}$.

HR1: Hardness ratio.

HR1_ERR: Hardness ratio error.

OFFAX: Off Axis Angle in arcmin.

RA_OPT: Best fit right ascension in decimal Degree units of the best CANDELS counterpart.

DEC_OPT: Declination in decimal Degree units of the best CANDELS counterpart.

m160: F160W AB magnitude.

Spec_z: Spectroscopic redshift from Santini et al. (2014).

Photo_z: Photometric redshift from Santini et al. (2014).

Photo_z_H: Photometric redshift from Hsu et al. (2014).

X11: Source ID in X11¹⁸.

H14: Source ID in Hsu et al. (2014).

6. GENERAL PROPERTIES OF THE X-RAY SAMPLE

Here we present a preliminary overview of the properties of newly detected X-ray sources while, a more complete analysis will be presented in a forthcoming dedicated paper. In the upper left panel of Fig. 10 left, we show the [0.5-10] keV flux of our detections vs the F160W magnitude of their counterparts for the whole sample and for the new detected sources. As expected, the new sources are fainter than the whole sample, and also their brightness distribution of their counterparts is peaked at fainter magnitudes. In particular the whole sample of counterparts has $\langle m_{F160W} \rangle = 23.1$, while for the new sources $\langle m_{F160W} \rangle = 24.3$.

In the upper-right panel of Fig. 10 we show the X-ray colors as a function of the [0.5-10] keV flux. The X-ray color, or hardness ratio, is defined as $HR = \frac{H-S}{H+S}$ where, H and S are the count rates in the [2-7] keV and [0.5-2] keV energy bands, respectively.

The whole sample has an average hardness ratio of ~ -0.1 (*green points*) corresponding to a power-law spectrum with photon index $\langle \Gamma \rangle = 1.4$. The *new* sources have a slightly harder average hardness ratio $\langle HR \rangle \sim 0.0-0.5$ (*blue points*). This difference, although marginally significant, suggests that the *new* population may include a large number of obscured AGN.

The luminosities of the low redshift sources are as low as $10^{40} \text{ erg s}^{-1}$ (see bottom right panel of Fig. 10) indicating that the bulk of the $z < 1$ population is due to star forming galaxies and low luminosity obscured AGN.

An updated catalog of X-ray sources detected in the CDFS with blind standard methods was recently assembled (Hsu et al. (2014)), merging various catalogs: X11, Luo et al. (2008), Virani et al. (2006) and Rangel et al. (2013). In the CANDELS area 11 sources are not detected by Hsu et al. (2014) (all of them in X11). Six out of 11 sources are recovered in our catalog. As a consequence, the Hsu et al. (2014) catalog contains 5 sources which were not detected neither by us nor by X11. Therefore the total number of bona fide X-ray sources in the CANDELS GOODS area is 789.

Finally, we cross correlated our catalog with the photo-z catalog presented by Santini et al. (2014), in the lower-left panel of Figure 10 we show the photo-z distribution for the *new* and *old* X-ray source population compared

with that of X11. Such a catalog has been derived by computing the weighted average of the Probability Distribution Functions (PDFs) obtained by several teams using galaxy templates. This could be a problem for some of our sources since their powerful X-ray emission indicates AGN activity and therefore a nuclear contamination of the SED. For these sources the photo-z may not be reliable however, since Hsu et al. (2014) measure the photo-z by including AGN contamination in the fit we included their photo-z for the sources in common. We note that the bulk of our *new* X-ray sources lie at $z \sim 1-3$ and, remarkably, we find 9 highly reliable (FLAG_ASSOC=1) candidates with photo-z ≥ 4 , 2 with Spec-z ≥ 4 (and photo-z < 4) and another 4 with photo-z ≥ 4 but FLAG_ASSOC=2 in the CANDELS catalog. We point out that source NID=624, detected on the tail of a bright off-axis X-ray source, could be a spurious detection. Eight of them are in common with the X11 and Giallongo et al. (2015) catalogs. In Table 3 we report all the high-z candidates and mark those already detected by Giallongo et al. (2015) and X11. The high-z candidates are likely to be AGN with luminosities of the order of $10^{43-43.5} \text{ erg s}^{-1}$. Another source in common with Giallongo et al. (2015) is CANDELS ID=29323 (NID=495) with photo-z=9.73 however, the photo-z of this source is dominated by artifacts in the SED and it is not reported in Table 3. The high-z candidate sources which are not in common with Giallongo et al. (2015) and X11 are in general (except one, NID624) faint and just above the threshold. Interestingly, Giallongo et al. (2015) detects more (22) candidate $z > 4$ X-ray sources; this is apparently in contrast with our findings. We have then searched our raw catalog, which includes sources down to $\mathcal{L} = 3$, and retrieved 17/22 sources within $2''$ from our X-ray centroid. Although found at low threshold we cannot exclude with our method, at a significance level of $\sim 95\%$ that these sources (at least in this band) are background fluctuations at the position of CANDELS galaxy. Therefore we can explain such a discrepancy with the fact that the two methods adopt different thresholds and different energy bands. In fact while we used standard energy ranges Giallongo et al. (2015) choose the energy band which could maximize the SNR. The analysis of the full *Chandra* data set, known as the 7 Ms, will provide further clues and will be the subject of a future investigation. Finally we want to point out that in the catalog of Hsu et al. (2014) none of our 7 high-z candidate in common with them has a photo-z > 4 . While this requires a deeper investigation, a similar result was found by Weigel et al. (2015) who did not find any $z > 5$ source in the same area.

7. CONCLUSION AND SUMMARY

In this paper we have presented a new X-ray source catalog in the GOODS-S area based on the 4 Ms *Chandra* CDFS data. For the first time we produced a catalog with both a maximum likelihood PSF fitting technique based on prior HST galaxy detections as well as an “a-posteriori” LR test to confirm the association. The method is tested through extensive Monte Carlo ray-tracing simulations using the state of art knowledge of the SFR- L_X scaling relation for star-forming galaxies and AGN population synthesis models for the CXB.

In this paper we developed and tested a technique

¹⁸ sources in the X11 supplementary catalog have been number with their ID+1000

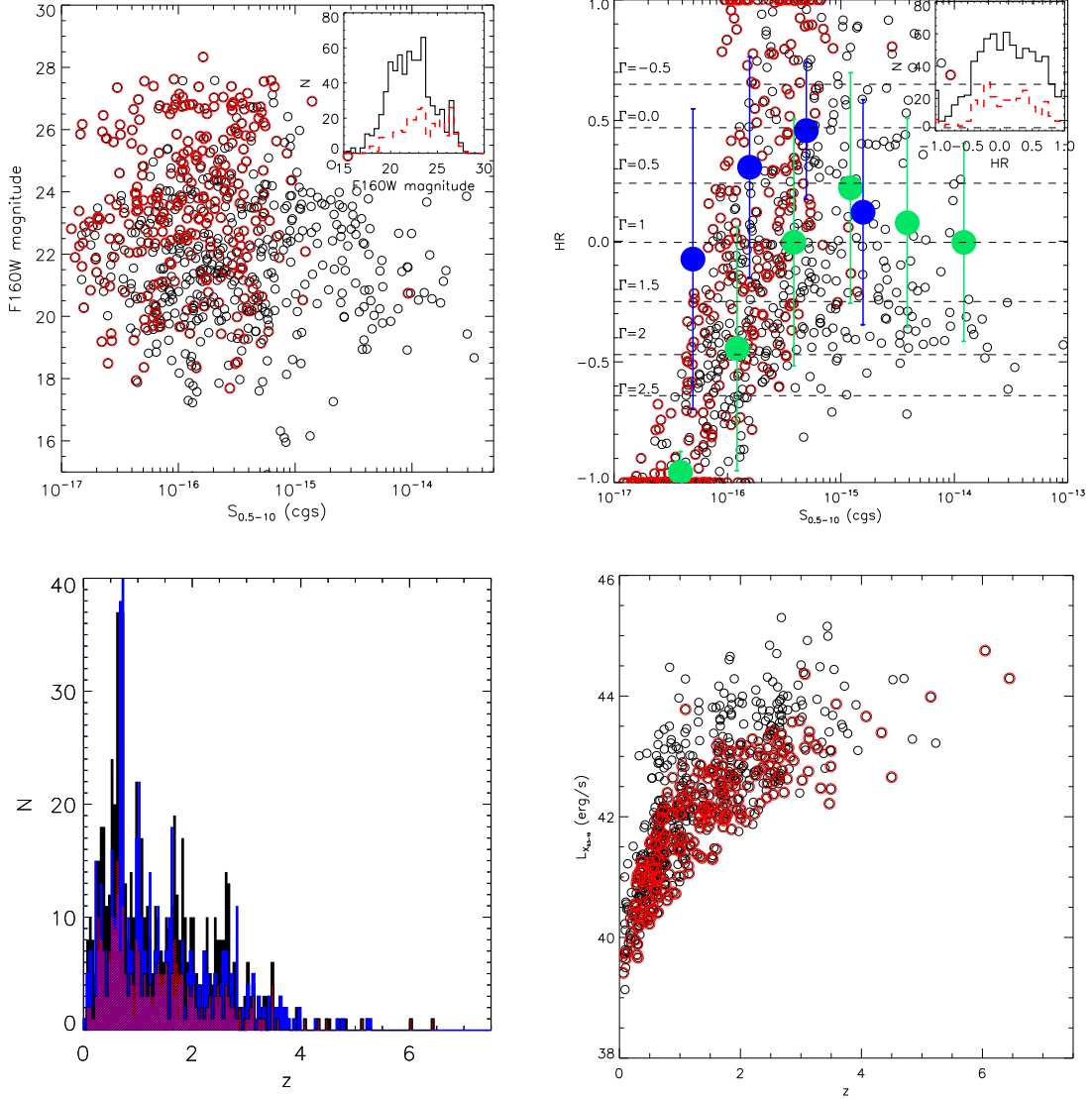


FIG. 10.— *Top left panel* The $S_{0.5-10}$ versus the F160W AB magnitude for the whole sample (black open circles) and for new sources (red open circles). The inset show the F160W AB magnitude distribution for the whole sample (black histogram) and for new sources (red histogram). *Top right panel* The $S_{0.5-10}$ versus HR for the whole sample (black open circles) and for new sources (red open circles). The horizontal dashed lines represent the expected HR for a power-law spectrum with varying spectral index $\Gamma = -0.5 - -2.5$ from top to bottom. The green filled circles are the average HR in $\Delta \text{Log}(S) = 0.25$ flux bin for the whole sample, while blue filled circles are the same but for new sources. *Lower left panel* : The photo- z distribution for the whole sample (black filled histogram) and for new sources (red filled histogram) compared with the fiducial redshift distribution of X11 (blue filled histogram). *Lower right panel* : the photo- z versus $L_{0.5-10}$ for the whole sample (black open circles) and for new sources (red open circles).

based on optical/near-infrared priors to fully exploit the deep observations in the *Chandra* Deep Field South. The detection of faint X-ray sources at the limit of the *Chandra* capabilities is based on two approaches. Recently, thanks to ultra-deep multiwavelength survey with HST, like CANDELS combined with high angular resolution of *Chandra* some authors proposed to use the entire three-dimensional data-cube (position and energy), and searching for X-ray counts at the position of high- z galaxies in the GOODS-South survey assuming that the angular resolution of *Chandra* is good enough to locate accurately the position of the X-ray sources.

These approaches complement the previously widely adopted one, based on either wavelets (see e.g X11) or PSF fitting (Puccetti et al. 2009) of candidates sources

selected among the most significant background fluctuations. The X-ray selected samples are then matched with optical/NIR catalogs and the actual counterpart of the X-ray sources are assigned using the LR techniques which balances the distance source/counterpart and the underlying magnitude distribution of the counterparts.

Here we applied both methods to the X-ray 4Ms data of the Goods-South region. We first performed a PSF fitting on a sample of HST-WFC3 selected galaxies down to a magnitude limit where we reasonably expect to identify most of the X-ray source counterparts. Our results, validated by simulations, indicate that using priors we can detect objects down to a likelihood threshold that is respect than in previous works. As a result, we end up increasing the number of faint sources detection (Fig. 4

TABLE 3
CANDIDATE $z > 4$ X-RAY SOURCES BASED ON PHOTO-Z.

NID	PRIOR_ID	FLAG_ASSOC	\mathcal{L}_{FULL}	FLUX_FULL	Spec_z	Photo_z	Photo_z_H	X11
624 ^b	28496	1	52.096638	1.39×10^{-15}	-9.0	6.045	-99.0	-99
306	4760	2	7.5424814	6.32×10^{-17}	-9.0	5.78	-99.0	-99
295 ^a	20765	1	9.3882885	5.73×10^{-17}	-9.0	5.229	2.6389	521
341	25825	2	5.7868	3.48×10^{-16}	-9.0	5.145	-99.0	-99
216 ^a	19713	1	9.819359	8.01×10^{-17}	-9.0	4.842	3.0113	392
572 ^a	4356	1	66.05208	8.66×10^{-16}	-9.0	4.703	1.7139	485
599 ^a	16822	1	230.46376	9.09×10^{-16}	-9.0	4.521	3.2327	371
59	4466	1	5.5986195	2.23×10^{-17}	-9.0	4.498	-99.0	-99
510 ^a	273	2	8.904563	5.91×10^{-16}	4.762	4.488	0.1374	403
272	14537	1	5.257827	1.33×10^{-16}	-9.0	4.331	-99.0	-99
400	24833	1	5.476905	2.84×10^{-16}	-9.0	4.079	-99.0	-99
575	24636	2	28.0794	6.68×10^{-16}	-9.0	4.054	3.699	602
238	4209	1	8.693058	6.63×10^{-17}	4.724	3.123	-99.0	-99
571	23382	1	31.888372	7.93×10^{-16}	4.379	2.294	2.4261	534

^aSource detected by Giallongo et al. (2015), Fiore et al. (2012).

^bPossibly spurious source on the tail of a bright offaxis X-ray source.

and Fig. 5).

We also performed a likelihood ratio analysis using well established techniques to associate the detected sources with the optical catalog. The overall result is that through the LR test we can confirm that among the $\sim 83\%$ of sources for which a secure match is found, at off-axis angles $< 4'$, the counterpart determined by the LR is coincident with the prior in $\sim 99\%$ of the cases. This fraction drops to 92-93% at larger off-axis angles. The prior is the actual counterpart of the identified sources, on average, in 96% of the cases. This observational finding is confirmed by extensive simulations. For the remaining 17% (i.e. 90 unsecure, 14 ambiguous, and 7 secure for which the prior and the LR counterpart do not match) we cannot draw any conclusion on the identity of the counterpart.

After fitting the X-ray centroid, the LR test suggests that the use of priors ensures the detection of the correct counterpart in at least 87% of the cases. For the remaining 13%, the X-ray centroid is significantly displaced from the optical source or the objects are at large ($> 4'$ off-axis angles. Although it is not always possible to firmly associate HST and *Chandra* sources without running a LR analysis, we note that at least for sources with FLAG_ASSOC=1 that the counterpart is coincident with the prior in 98% of the cases if we consider the inner portion of the field of view $\theta_{offaxis} < 4'$. At larger off-axis angles this fraction drops to 92%.

Our method significantly improves the efficiency in the detection of faint X-ray sources in deep X-ray surveys by taking advantage of the precise HST positions. Indeed 257 new X-ray sources are discovered down to a flux of $\sim 1(8) \times 10^{-17}$ erg cm $^{-2}$ s $^{-1}$ in the [0.5-2] keV ([0.5-10] keV) energy band.

The final catalog contains 698 X-ray sources selected in the [0.5-7] keV energy range. 552 have a secure match with the CANDELS catalog. By cross-matching the current catalog with those published in the literature we were able to estimate that the number of unique X-ray sources in the CANDELS GOODS-S area sums up to 789. Based on photo-z and a few spectro-z, 15 candidates high-redshift $z > 4$ AGN are identified. Six of them are in common with Giallongo et al. (2015), the counter-

part of 4 FLAG_ASSOC=2 sources is ambiguous. While the discrepancy with previous results (Giallongo et al. 2015) can be explained as due to different approaches and thresholds adopted, we conclude that the actual number of X-ray selected AGN at $z > 5$ remains very sensitive to the details of the analysis and ultimately needs deeper and better data to be robustly measured. Also, since other authors using different approaches obtain different results than those reported in the official catalog (e.g. Hsu et al. 2014; Weigel et al. 2015), we want to point out that a discussion of the photo-z quality included in our catalog is beyond the scope of this paper and it will be discussed elsewhere.

Indeed, the method presented and extensively discussed in this paper may be obviously extended to many other X-ray surveys where deep optical/NIR HST ancillary data are available and may significantly boost the legacy value of these programs. We point out that the most rewarding scientific return of the method is obtained if it is applied to surveys designed to have a constant PSF and a sharp core, like the COSMOS Legacy and the UDS *Chandra* fields.

NC acknowledges the Yale University YCAA Prize Postdoctoral Fellowship program. We acknowledge the contribution of the EC FP7 SPACE project ASTRODEEP (Ref. No: 312725). ASTRODEEP is a FP7-funded coordinated and comprehensive program of i) algorithm/software development and testing; ii) data reduction/release, and iii) scientific data validation/analysis aimed at making Europe the world leader in the exploitation of the deepest multi-frequency astronomical survey data. NC acknowledges Marcella Brusa and Francesca Civano for discussions about the LR technique. NC thanks Roberto Gilli and Cristian Vignali for insightful discussions. NC thanks Mara Salvato for discussions about photo-z quality. NC thanks Hermann Brunner for his valuable assistance with *cmldetect*. JSD acknowledges the support of the European Research Council through the award of an Advanced Grant. NC kindly acknowledges M.M. Lozio for the useful discussions. We especially thank the anonymous referee for the useful comments that significantly improved this paper.

REFERENCES

- Aird, J., Nandra, K., Laird, E. S., et al. 2010, MNRAS, 401, 2531
 Basu-Zych, A. R., Lehmer, B. D., Hornschemeier, A. E., et al. 2013, ApJ, 762, 45

- Brusa, M., Comastri, A., Daddi, E., et al. 2005, *A&A*, 432, 69
- Brusa, M., Zamorani, G., Comastri, A., et al. 2007, *ApJS*, 172, 353
- Cappelluti, N., Hasinger, G., Brusa, M., et al. 2007, *ApJS*, 172, 341
- Cappelluti, N., Kashlinsky, A., Arendt, R. G., et al. 2013, *ApJ*, 769, 68
- Cappelluti, N., Ranalli, P., Roncarelli, M., et al. 2012, *MNRAS*, 427, 651
- Cash, W. 1979, *ApJ*, 228, 939
- Cileigi, P., Zamorani, G., Bondi, M., et al. 2005, *A&A*, 441, 879
- Craddace, R. G., Hasinger, G. R., & Schmitt, J. H. 1988, *European Southern Observatory Conference and Workshop Proceedings*, 28, 177
- Civano, F., Elvis, M., Brusa, M., et al. 2012, *ApJS*, 201, 30
- Dickey, J. M., & Lockman, F. J. 1990, *ARA&A*, 28, 215
- Daddi, E., Cimatti, A., Renzini, A., et al. 2004, *ApJ*, 617, 746
- Ebrero, J., Carrera, F. J., Page, M. J., et al. 2009, *A&A*, 493, 55
- Fabbiano, G. 1989, *ARA&A*, 27, 87
- Finoguenov, A., Tanaka, M., Cooper, M., et al. 2015, *arXiv:1501.03506*
- Fiore, F., Puccetti, S., Grazian, A., et al. 2012, *A&A*, 537, AA16
- Giallongo, E., Grazian, A., Fiore, F., et al. 2015, *arXiv:1502.02562*
- Gilli, R., Comastri, A., & Hasinger, G. 2007, *A&A*, 463, 79
- Grazian, A., Castellano, M., Koekemoer, A. M., et al. 2011, *A&A*, 532, A33
- Guo, Y., Ferguson, H. C., Giavalisco, M., et al. 2013, *ApJS*, 207, 24
- Hasinger, G. 2008, *A&A*, 490, 905
- Hickox, R. C., & Markevitch, M. 2006, *ApJ*, 645, 95
- Hsu, L.-T., Salvato, M., Nandra, K., et al. 2014, *ApJ*, 796, 60
- Lehmer, B. D., Xue, Y. Q., Brandt, W. N., et al. 2012, *ApJ*, 752, 46
- Kashlinsky, A., Arendt, R. G., Ashby, M. L. N., et al. 2012, *ApJ*, 753, 63
- Kennicutt, Robert C., J. 1998, *ARA&A*, 36, 189
- Krumpe, M., Miyaji, T., Brunner, H., et al. 2015, *MNRAS*, 446, 911
- Luo, B., Bauer, F. E., Brandt, W. N., et al. 2008, *ApJS*, 179, 19
- Madau, P., Haardt, F., & Dotti, M. 2014, *ApJ*, 784, LL38
- Mineo, S., Gilfanov, M., & Sunyaev, R. 2012, *MNRAS*, 419, 2095
- Mineo, S., Gilfanov, M., Lehmer, B. D., Morrison, G. E., & Sunyaev, R. 2014, *MNRAS*, 437, 1698
- Miyaji, T., Hasinger, G., Salvato, M., et al. 2015, *arXiv:1503.00056*
- Mortlock, D. J., Warren, S. J., Venemans, B. P., et al. 2011, *Nature*, 474, 616
- Applied Multivariate Statistical Analysis, 6th Edition, Richard A. Johnson & Dean W. Wichern 2007
- Puccetti, S., Vignali, C., Cappelluti, N., et al. 2009, *ApJS*, 185, 586
- Ranalli, P., Comastri, A., & Setti, G. 2005, *A&A*, 440, 23
- Rangel, C., Nandra, K., Laird, E. S., & Orange, P. 2013, *MNRAS*, 428, 3089
- Santini, P., Ferguson, H. C., Fontana, A., et al. 2014, *arXiv:1412.5180*
- Sargent, M. T., Béthermin, M., Daddi, E., & Elbaz, D. 2012, *ApJ*, 747, L31
- Salvato, M., Ilbert, O., Hasinger, G., et al. 2011, *ApJ*, 742, 61
- Schreiber, C., Pannella, M., Elbaz, D., et al. 2015, *A&A*, 575, AA74
- Sutherland, W., & Saunders, W. 1992, *MNRAS*, 259, 413
- Treister, E., Schawinski, K., Volonteri, M., & Natarajan, P. 2013, *ApJ*, 778, 130
- Ueda, Y., Akiyama, M., Hasinger, G., Miyaji, T., & Watson, M. G. 2014, *ApJ*, 786, 104
- Vito, F., Gilli, R., Vignali, C., et al. 2014, *MNRAS*, 445, 3557
- Virani, S. N., Treister, E., Urry, C. M., & Gawiser, E. 2006, *AJ*, 131, 2373
- Volonteri, M. 2010, *A&A Rev.*, 18, 279
- Weigel, A. K., Schawinski, K., Treister, E., et al. 2015, *MNRAS*, 448, 3167
- Williams, R. J., Quadri, R. F., Franx, M., van Dokkum, P., & Labbé, I. 2009, *ApJ*, 691, 1879
- Xue, Y. Q., Luo, B., Brandt, W. N., et al. 2011, *ApJS*, 195, 10
- Yue, B., Ferrara, A., Salvaterra, R., Xu, Y., & Chen, X. 2013, *MNRAS*, 433, 1556